Wind Turbine Rotor Blade Testing by Dual-Energy Laminography

David SCHUMACHER [1], Dongsheng OU [2], Carineh GHAFAFIAN [1], Uwe ZSCHERPEL [1], Volker TRAPPE[1]
[1] Bundesanstalt für Materialforschung und –prüfung (BAM), Berlin, Germany
[2] Department of Engineering Physics, Tsinghua University, Beijing, China
Contact e-mail: David.Schumacher@bam.de

Abstract. Modern wind turbine rotor blades consist of sandwich shell segments made from glass fiber reinforced polymers. During manufacturing, defects can arise which could lead to failure of the whole component under dynamic mechanical and thermal loads. Hence during operation defects can arise which, if detected, can be repaired locally and in-situ by applying repair patches instead of taking the whole rotor blade down and repair it remotely. This method is much more time and cost effective, since the shut-down time of the energy converter is limited to a minimum. These repair patches can, however, also lead to new defects if not applied optimally. Therefore, it is necessary to control the quality of the repair patches to ensure the best possible restoration of structural integrity of the component. As a rotor blade is an object with a large aspect ratio, X-ray laminography is predestined to provide 3D information of the objective volume. To enhance the amount of information gained from laminographic reconstruction, we use in this study a photon counting and energy discriminating X-ray detector and apply a material decomposition algorithm to the data. By inherently separating the incident spectra within the detection process into two distinct energy bins, the basis material decomposition can provide material resolved images. Choosing glass and epoxy resin as basis materials and numerically solving the inverse dual-energy equation system, the reconstructed laminographic datasets contain highly valuable information about the distribution of the basis materials within the structure. Furthermore, cross- artifacts arising from the limited angle of the projection data can be reduced by this method which allows to investigate structures that were hidden underneath the artefacts.

Introduction

Non-destructive testing of wind turbines is important in the life cycle maintenance of these systems, since they are subjected to high dynamic loads and cyclic fatigue. Offshore systems are exposed to especially extreme mechanical and thermal loads due to higher wind and temperature variations [1]. The segment of a wind turbine blade investigated in this study consists of a sandwich shell segment made from glass fiber reinforced polymer (GFRP), a standard material of wind turbine blades. Each sandwich segment contains a polyvinyl chloride (PVC) foam core with two layers of biaxial (BIAX) glass fiber plies on each side [2, 3]. The shells of turbine blades are manufactured per hand. The high amount of manual fabrication facilitates the formation of manufacturing flaws which have the potential to grow

into harmful defects due to the cyclic loading, hence compromising the integrity of the turbine blade or the whole system. The most likely and severe damages are structural failure initiating cracks in the blade shell that occur long before the maximum service life time of 20 years is reached [1].

The in-service detection and validation of flaws in turbine blades is still being improved to-date. In case a flaw has been located and identified, special techniques exist to locally repair the defective volume and thus restore the component design lifespan. Due to time, environmental constraints and ease of availability, however, the quality of the repairs often remains unmonitored in the field. As the repairs are installed per hand on the ropes, variations such as gaps between repair and parent foam, for instance, could result in resin channels. Such imperfections in the repair patches could be further propagated during service and thus turn into potential sources for damage initiation.

To find out if and how sustainably a repair patch can restore the design lifespan of a damaged wind turbine blade, the BAM is conducting research project in which GFRP sandwich shell specimens are manufactured and instantly repaired with various predefined methods. The repaired parts are tested under cyclic load to simulate the fatigue behavior of these specimens [4].

In this study, an X-ray dual-energy laminography technique addresses this matter, enabling a detailed quality assurance imaging method of repair patches installed on blade shells. Like CT, laminography can deliver a three-dimensional volume of the investigate part, but due geometric constrains the depth information is limited [5]. To enhance the reliability of this NDT technique, the laminography is extended by a material resolution gained from spectral information of the detected X-ray photons. Therefore, a photon counting and energy discriminating X-ray detector (PCD) in combination with a basis material decomposition (BMD) algorithm is used. This BMD algorithm enables to separate between two predefined base materials (here: glass and epoxy resin) in the resulting data set.

1. Methods

1.1 Samples

The test specimens were produced as a curved sandwich structure with SAERTEX GFRP laminate face sheets and an AIREX C70.55 polyvinyl chloride (PVC) foam core, representing a portion of a wind turbine rotor blade shell. Two layers of ±45° 812 g/m^2 non-crimp glass fiber fabric were used as face sheets, with additional 1200 g/m^2 unidirectional reinforcement layers in the clamping region to maintain homogeneity in the specimen thickness, illustrated in **Fig. 1**. The vacuum-assisted resin infusion (VARI) process was utilized to produce the shell specimens with the RIMR135/RIMH137 epoxy resin system from Hexion. Specimens were cured first at room temperature for 48 hours, then for 15 hours at an elevated temperature of 80°C.

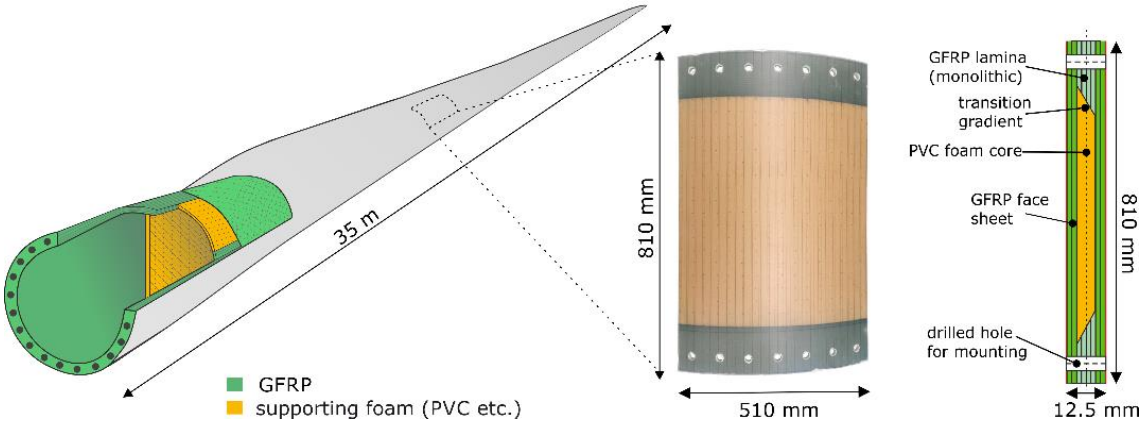

Fig. 1: Sandwich test specimens designed as a representative portion of a rotor blade shell. Side view (far right) shows the ±45° GFRP face sheets, as well as the monolithic clamping region at the top and bottom.

The specimens were then repaired with an adhesively bonded patch, a method often utilized on composite materials, especially in the aerospace industry, where the lost load path is replaced with a new material that is joined to the parent structure [6, 7]. The specimen examined in this study was repaired with an external bonded repair, a relatively quick and simple method often used to repair blade shells, illustrated in **Fig. 2**. This method involves removing the damaged region, then cleaning and applying a filler material and adhesive, upon which the external repair plies are then placed. The loads are thus transferred over and around the damage due to the repair patch, with a decrease in localized stress concentration at the damage boundaries [6]. The shell specimen was repaired entirely by hand, as is done with rotor blade repairs in the field.

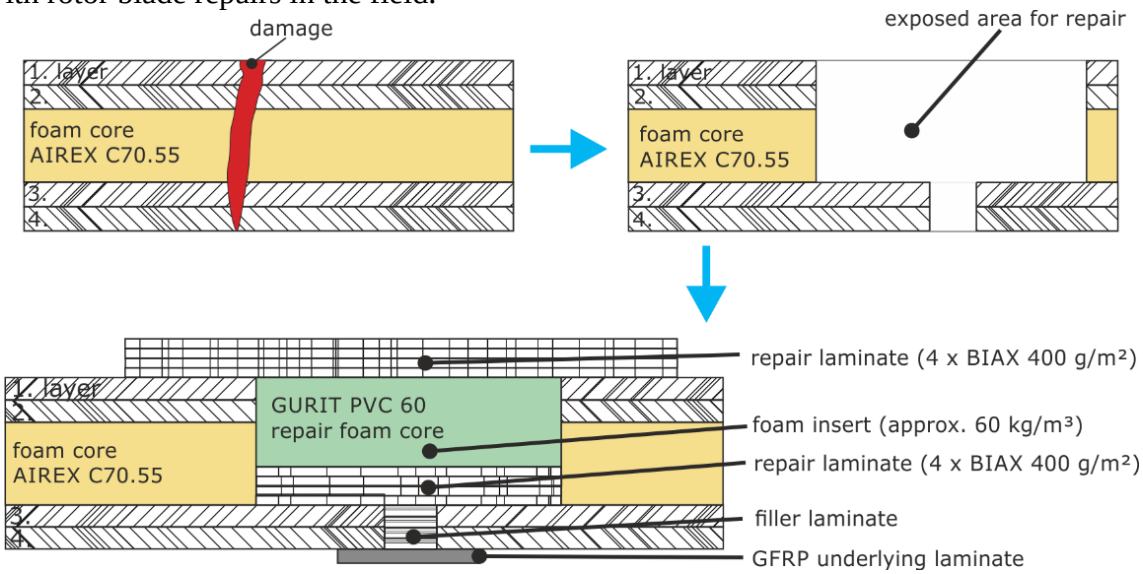

Fig. 2: External bonded repair patch schematic, as applied to sandwich specimen in this study.

The adhesively bonded specimen was then cyclically tested under uniaxial tensile-compressive load (R = -1) to study the effect of the repair patch on the damage and failure mechanisms of the structure.

1.2 Photon Counting Detectors

The direct detection principle of photon counting detectors (PCDs) differs from common indirect detector technology by renouncing scintillation layers (e.g. CsI or Gd_2O_2S) in which the incident X-rays are converted to visible light before the optical photons can be detected (**Fig. 3**). PCDs are based on semi-conductor materials (e.g. CdTe or Si) in which the incident

X-rays are directly converted into electrical signals. Since the amount of charge generated by an X-ray photon is directly proportional to its energy, PCDs are able to determine the energy of the incident X-ray photons and therefore generate spectral information. Additionally, the absence of optical scattering (from the scintillation layer) leads to a much lower inner unsharpness (basic spatial resolution equals usually pixel size) and therefore much sharper images. [8–10]

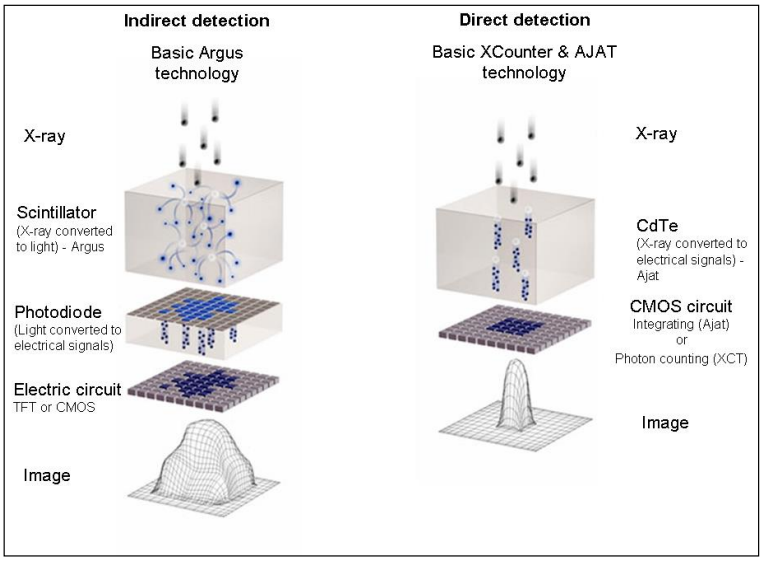

Fig. 3: Comparison between indirect (left) and direct (right) detection of X-rays[1]

The PCD used in this study is based on CdTe monocrystalline. The spectral information is generated by comparing the charge pulse height (i.e. amount of charge) of a detected event with a predefined threshold. Only if the detected pulse height is larger than the threshold set, the counter is incremented. The number of pulse height comparators per pixel gives the number of available energy bins. In the present detector, each pixel is equipped with two pulse height discriminators resulting in two energy bins per pixel (**Fig. 4**). The first threshold cuts off background noise from the detector electronics and the second threshold divides the detected spectrum into a low energy (le) and a high energy (he) part. This spectral information can be used to generate material specific information from the investigated object.

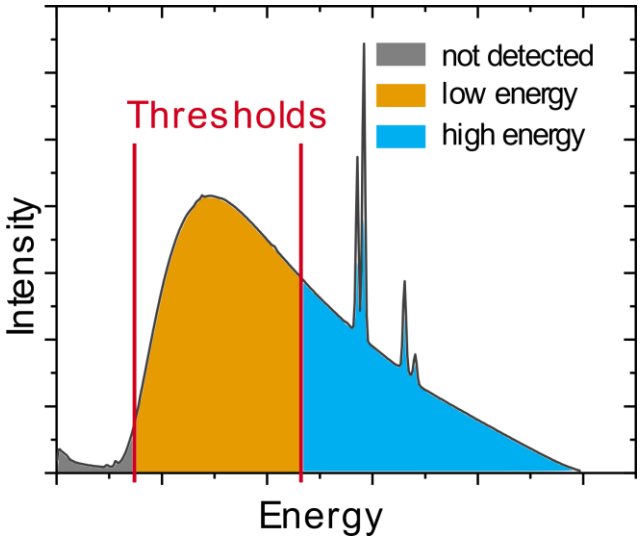

Fig. 4: Principle of spectrum splitting by internal energy thresholding of the PCD.

[1] from: http://directconversion.com/technology/

1.3 Laminography

The large aspect ratio (approximately 1:40) of the shell segments does not allow CT to be used to investigate the 3D structure of the volume. Instead, computed laminography is used to reveal the 3D information of the repair patches. Computed laminography is a technique which was developed in the 1930s by B. G. Z. des Plantes [11] for medical purposes. There exist many types of laminographic techniques which are mainly distinguished by the characteristic trajectory. “Rotational laminography” or “swing laminography” are based on an inclination of the sample relative to source and detector. Translational techniques like “co-planar translational laminography” which is used in this study are based on a relative linear movement between sample and source and/or detector. In all techniques, projection images are acquired under different angles of incidence (AOI) from which depth information can be reconstructed.

In the co-planar translational laminography, the X-ray tube executes a linear movement parallel to the horizontal pixel lines of the PCD. During this manipulation a sequence of projection images is acquired by the PCD where each projection image represents the object from a different AOI. After acquisition, the stack of projection images is passed to a *weighted filtered shift-average* reconstruction algorithm [12] which delivers a three-dimensional data set of the investigated object.

Fig. 5 depicts the principle of a co-planar translational laminography. The geometric constraints in **Fig. 5**b show, that due to the max. AOI α and restrictions in source-detector distance (SDD) and object-detector distance (ODD), the achievable resolution in the resulting data set is limited.

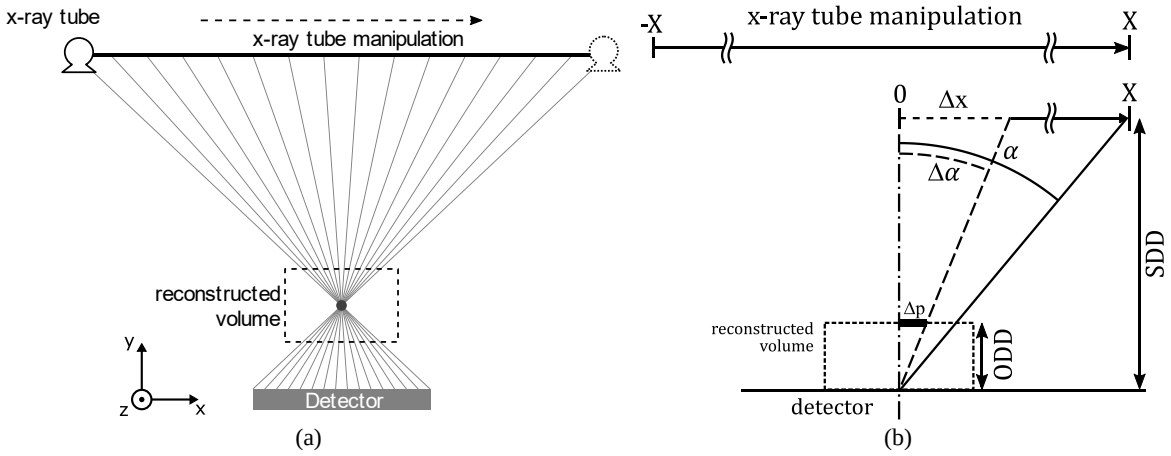

Fig. 5: (a) Principle of co-planar translational laminography to reconstruct a three-dimensional volume. (b) The geometric constraints, especially the limited angle of incidence α and the source-detector-distance (SDD) or object-detector distance (ODD), restrict the achievable resolution in the data set.

As the co-planar translational laminography intrinsically implies a limited view due to the limited AOI, artefacts arise after reconstruction. The amount and intensity of those artefacts is mainly depending on the maximum AOI and the number of projection images acquired during the scan. As a result of the maximum AOI, cross-artefacts may arise in the reconstructed data set which impede the analysis or (automated) segmentation of defective volume. By appropriate filtering of the projection data, the representation of cross-artefacts may be reduced in the final data set but the depth information will be further distorted. [5, 13]

Fig. 6 and **Tab. 1** show the setup and corresponding radiographic parameters for the dual-energy laminography on the repaired and cyclically loaded sandwich shell segments.

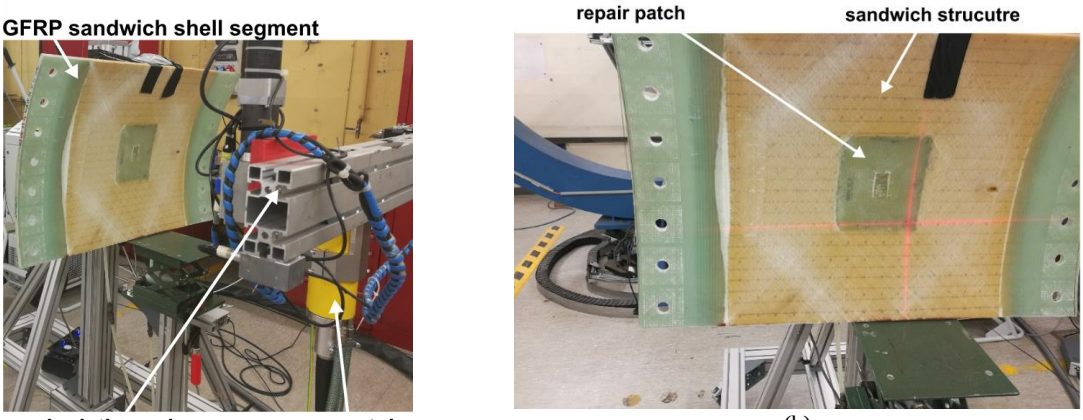

(a) (b)

Fig. 6: (a) Setup for dual-energy laminography on a GFRP sandwich shell segment of a wind turbine rotor blade. (b) The repair patch in the middle of the sandwich structure.

Tab. 1: Parameters for dual-energy laminography on a GFRP sandwich shell segment.

tube voltage[kV]	100
tube power [W]	230
spectrum filtering [mm Cu]	1.0
detector type	photon counting
sensor material	CdTe
sensor thickness [mm]	0.75
pixel size [mm]	0,1
detector area [mm²]	102.4 x 51.2
frame rate [Hz]	10
frames per projection	40
exposure time per projection [s]	4
No. of projections	971
max. AOI	± 40.3°
threshold *le*	~21 *keV*
threshold *he*	~52 *keV*

1.4 Basis Material Decomposition

A method to process the spectral information resulting from the internal energy thresholding of the PCD, is the basis material decomposition (BMD) which was developed by Alvarez and Macovski in the 1970s for medical purposes [14]. The BMD is not specific for PCDs, but since numerous energy bins per projection can be acquired within a single shot and be used for a material reconstruction, PCDs are advantageous for CT or laminographic applications.

The BMD uses the spectral information from the projection data to gain material specific images. The aim is to reconstruct the material thicknesses of two predefined basis materials by measuring the *le* and *he* intensities in the X-ray projection images.
In the simplified monoenergetic case of a transmission measurement of two materials i=1, 2 with thicknesses t_1 and t_2, the log. intensity according to Lambert-Beers law is:

$$\ln\left(\frac{I}{I_0}\right) = -\mu_1 t_1 - \mu_2 t_2 \quad (1)$$

Where I is the measured attenuated intensity, I_0 is the unattenuated intensity and μ_i is the attenuation coefficient of the corresponding material i.
If now two energy bins $j = le, he$ are defined, the following equation system can be formulated:

$$\begin{cases} I^{le}(t_1, t_2) = \int_{E_{min}^{le}}^{E_{max}^{le}} I_0(E)\, e^{-\mu_1(E)t_1 - \mu_2(E)t_2}\, dE \\ I^{he}(t_1, t_2) = \int_{E_{min}^{he}}^{E_{max}^{he}} I_0(E)\, e^{-\mu_1(E)t_1 - \mu_2(E)t_2}\, dE \end{cases} \tag{2}$$

The measured intensities I for each energy bin j are depending on the penetrated material thicknesses t of the two basis materials and the energy E. For this polychromatic case, the log. intensity p^j for each energy bin j and measured in each projection image can be expressed by:

$$p^j(t_1, t_2) = -\ln\left(\frac{\int_{E_{min}^j}^{E_{max}^j} I_0(E)\, e^{-\mu_1(E)t_1 - \mu_2(E)t_2}\, dE}{\int_{E_{min}^j}^{E_{max}^j} I_0(E)\, dE}\right) \tag{3}$$

This non-linear relation between the measured intensities p and the penetrated thicknesses t_i can now be approximated for each energy bin j by an appropriate function. This yields an equation system with a matrix of material thicknesses $\mathbb{T}$ and the measured log. intensities as the solution vector $\vec{p}$:

$$\vec{p} = \mathbb{T} \cdot \vec{c} \tag{4}$$

The coefficient vector $\vec{c}$ for this calibration system needs to be determined by known sampling points (i.e. material thicknesses). Depending on the application and positions of the sampling points, different functions may be chosen. In literature, commonly polynomials of degree n or conic functions are proposed [14–16], e.g.:

$$p^j = c_0 + c_1 t_G + c_2 t_E \tag{5}$$

$$p^j = c_0 + c_1 t_G + c_2 t_E + c_3 t_G^2 + c_4 t_G t_E + c_5 t_E^2 \tag{6}$$

$$p^j = \frac{c_0 + c_1 t_G + c_2 t_E + c_3 t_G^2 + c_4 t_G t_E + c_5 t_E^2}{1 + c_6 t_G + c_7 t_E} \tag{7}$$

with

$$\vec{c} = \begin{cases} \vec{a} & \text{für} \quad p^{le} \\ \vec{b} & \text{für} \quad p^{he} \end{cases} \tag{8}$$

Since in the projection images the intensities p^j are given (i.e. measured) and the combination of penetrated material thicknesses t_1, t_2 is searched, the inverse of the calibration system needs to be determined:

$$\vec{t} = \mathbb{P} \cdot \vec{c}^* \tag{9}$$

A (numerical) solution of this measurement system reveals the combination of basis material thicknesses t_1, t_2 for each measured combination of p^{le}, p^{he}. The relation between calibration and measurement system is shown in **Fig. 7**.

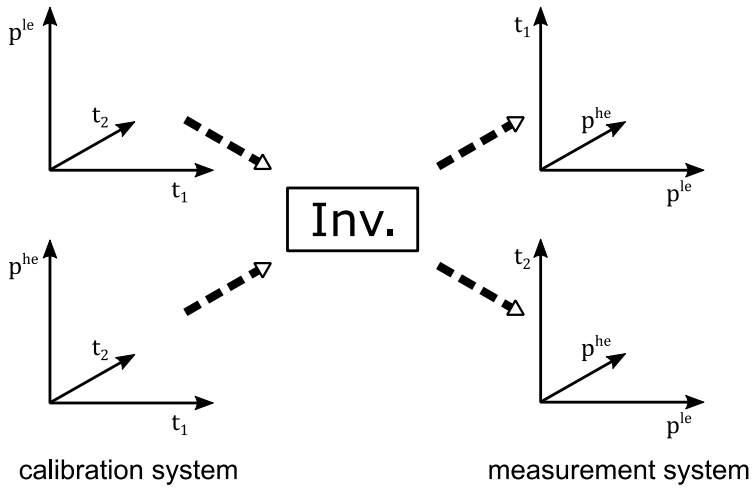

Fig. 7: Relation between calibration and measurement system of the BMD.

This algorithm is used to reconstruct the material thicknesses of glass (representing glass fibers) and epoxy resin based on the energy specific projection images of the laminographic scan in advance of the three-dimensional reconstruction.

2. Results and Discussion

To create a calibration system (described by Eq. 4), the *le* and *he* log. intensities are measured at different penetrated thickness combinations of glass and pure epoxy resin. The resulting sampling points are plotted in **Fig. 8**.

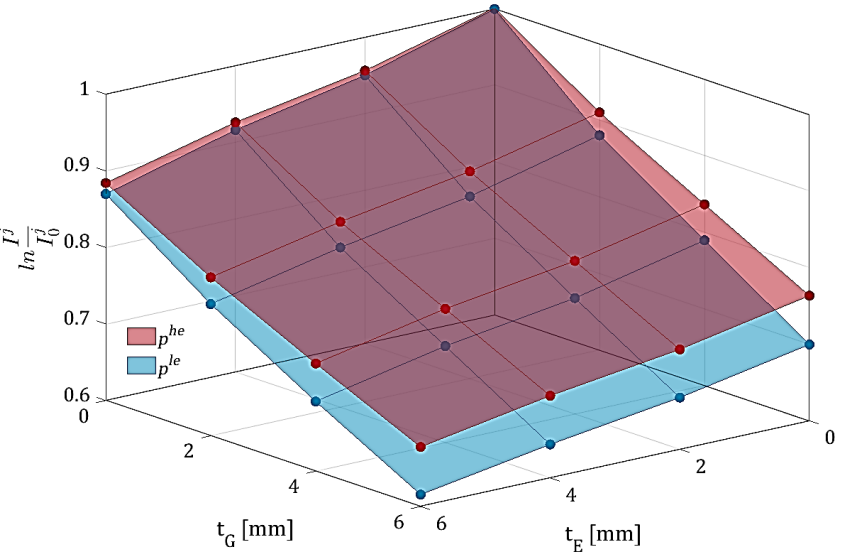

Fig. 8: Calibration system of an example pixel for the BMD of glass (G) and epoxy resin (E) and two distinct energy bins (*le* and *he*).

For reasons of simplicity and stability of the equation system, each of these planes (*le* and *he*) is fitted by a polynomial of degree 1 (Eq. ()). The inverse functions of these fits yield the measurement systems which can be used to calculate the present material thicknesses of glass or epoxy resin for a given combination of measured *le* and *he* intensities (**Fig. 9**).

(a)

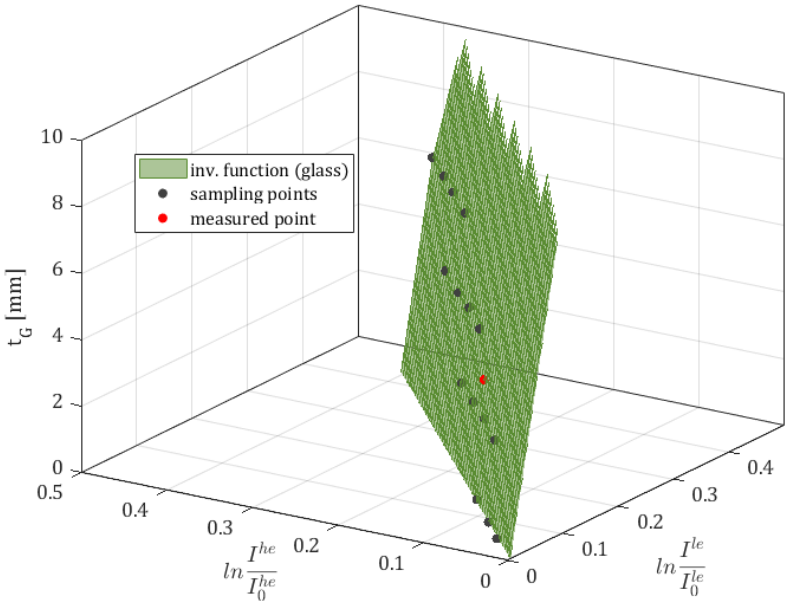

(b)

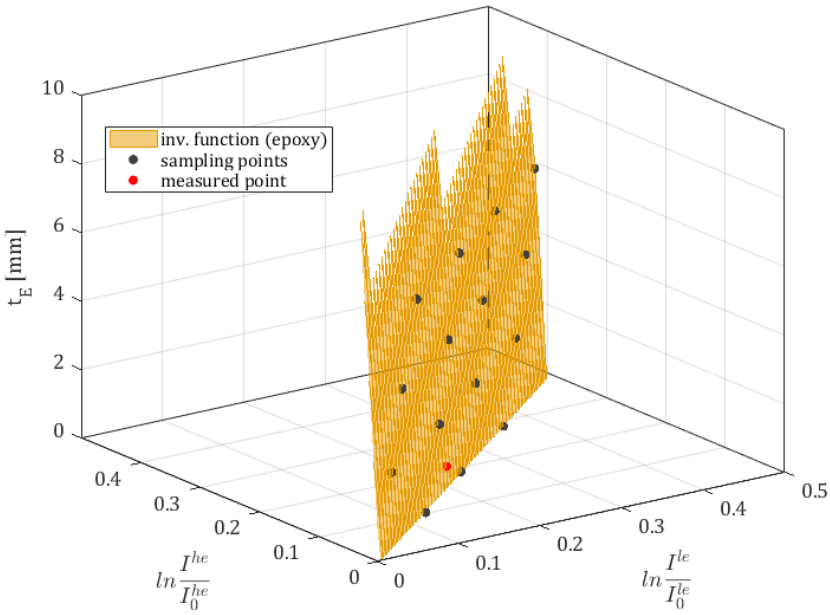

Fig. 9: Inverse fitting functions of an example pixel to calculate the material thicknesses of (a) glass and (b) epoxy resin for a given combination of measured intensities in the low and high energy bin. The block dots represent the sampling points and the red dot represents the measured *le* and *he* combination and hence the resulting material thickness in this pixel.

The results of the dual-energy laminography using a BMD to reconstruct the material thicknesses of glass and epoxy resin are shown in Figures 10 – 13.
Each of the Figures 10 – 12 represents another layer at the same lateral position in the reconstructed 3D volume. The subfigures contain the conventional laminography result (without BMD) next to the laminographies with the reconstructed basis materials glass and epoxy resin. The higher the intensity in the BMD data sets, the higher the amount of the corresponding basis material in this position.

Fig. **10** represents a slice close to the front surface of the sandwich shell segment. The intensive artefacts in case of the conventional laminography (Fig. **10**a) impede an analysis of these and the surrounding locations. These artefacts are suppressed by the BMD due to material selective reconstruction. The fine bright lines in Fig. **10**a could be misinterpreted as glass fibers, but Fig. **10**b reveals that only bundles of fibers and the gaps in-between can be resolved because the spatial resolution of the detector is too high to resolve single fibers. The epoxy resin data set in **Fig. 10**c shows dark spots which correspond to voids in the epoxy resin. The large number of voids in this slice cannot be recognized in **Fig. 10**a due to the overlapping material information.

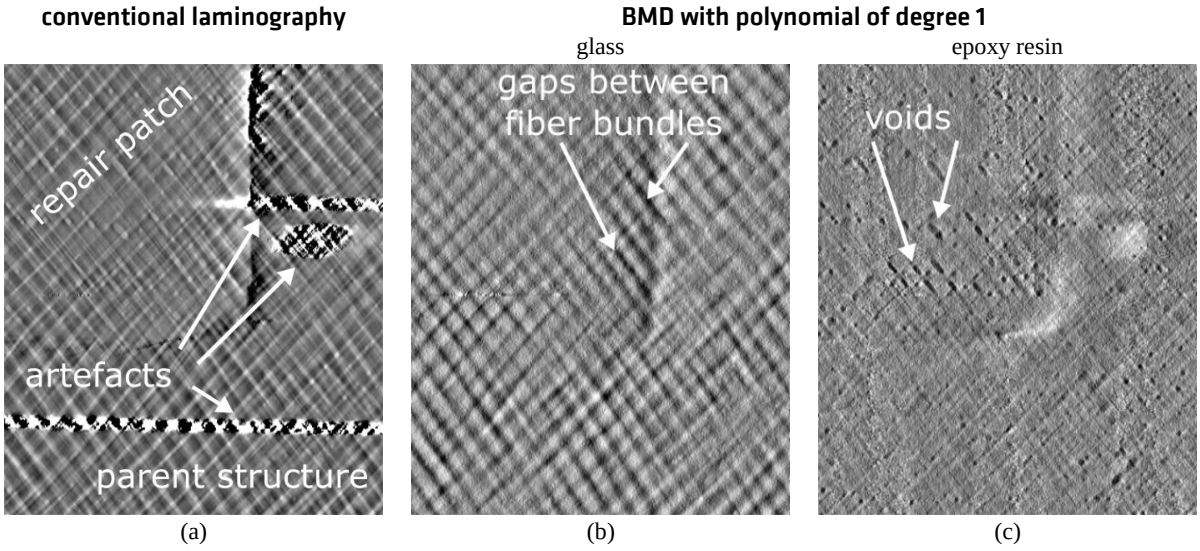

Fig. 10: Reconstructed slice close to the front surface of the sandwich shell segment. (a) Conventional laminography and the result of the BMD for (b) glass and (c) epoxy resin. Bright areas indicate a high amount of the present basis material.

Fig. 11 represents a slice in the middle of the sandwich shell segment where no glass fibers and rather only foam are present. Due to the artefacts in case of the conventional laminography (**Fig. 11**a) it is not clear, whether the edge of the repair patch and the drill hole are completely filled with resin or not. The epoxy resin reconstruction reveals, that the hole is homogeneously filled with resin, but the outer edge of the repair patch is not. The boundary of the repair patch consists partially of foam where an evenly filled resin channel was supposed to be. This indicates an insufficient connection between patch and parent structure which can be the origin of future failure initiation.

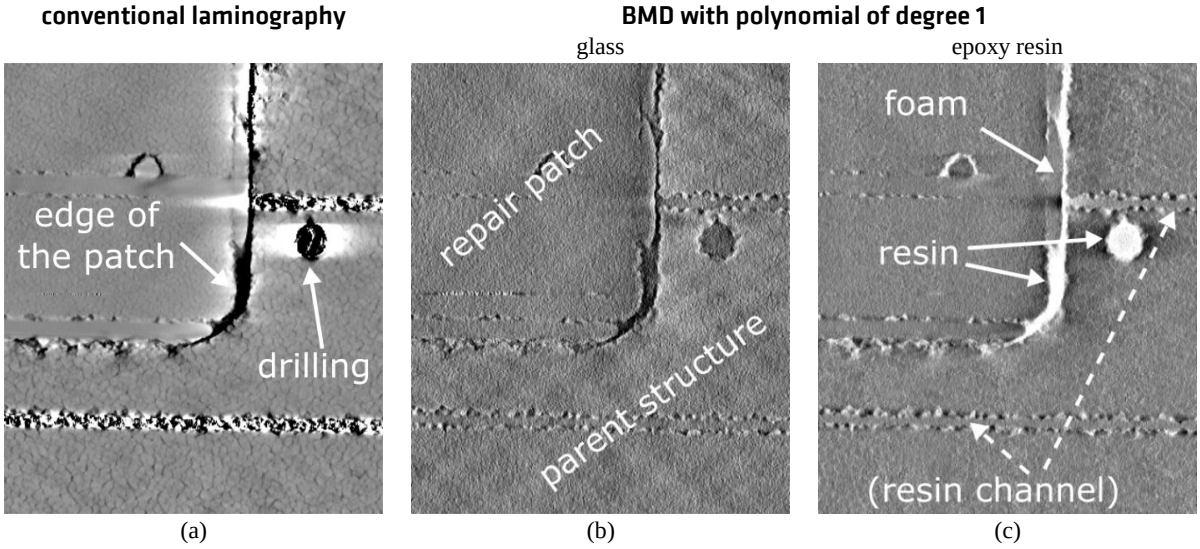

Fig. 11: Reconstructed slice in the middle of the sandwich shell segment. (a) Conventional laminography and the result of the BMD for (b) glass and (c) epoxy resin. Bright areas indicate a high amount of the present basis material.

Another slice close to the back surface of the sandwich shell segment is represented in **Fig. 12**. It shows that an additional layer of glass fiber fabric which was used for the repair patch, since in Figures 12a and 12b only the area of the repair patch indicates glass fiber bundles. The parent structure is free of glass fibers in this slice. **Fig. 12**c reveals that both, the edge of the repair patch and the drill hole are evenly filled with resin in this slice.

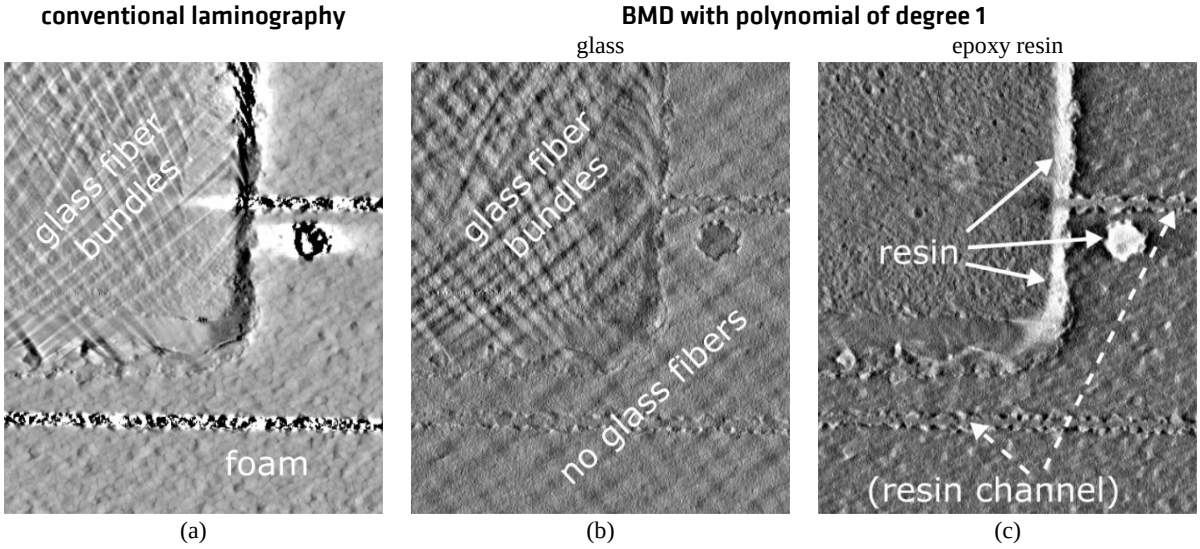

Fig. 12: Reconstructed slice close to the back surface of the sandwich shell segment. (a) Conventional laminography and the result of the BMD for (b) glass and (c) epoxy resin. Bright areas indicate a high amount of the present basis material.

The representation of the reconstructed volume in orthogonal slices allows to investigate the structure in more detail. Digital cross-sections of the conventional laminography and the epoxy resin reconstruction in **Fig. 13** show how the cross-artefacts are being suppressed by the BMD. In case of the conventional laminography (**Fig. 13**a), the artefacts overlay parts of the structure. Especially in the XY-plane, the artefacts of the drilled hole overlay a large part of the cross-section which impedes a distinct evaluation of the integrity of the component. In the epoxy resin reconstruction of the BMD (**Fig. 13**b), the XY-plane reveals a homogeneously resin filled drilled hole. The XY- and XZ-plane likewise reveal that the edge of the repair patch is not filled with resin across the entire depth of the component. Close to

the front surface (in y-direction), parts of the resin channel contain a piece of foam, signifying that the repair patch is not homogeneously surrounded by resin.

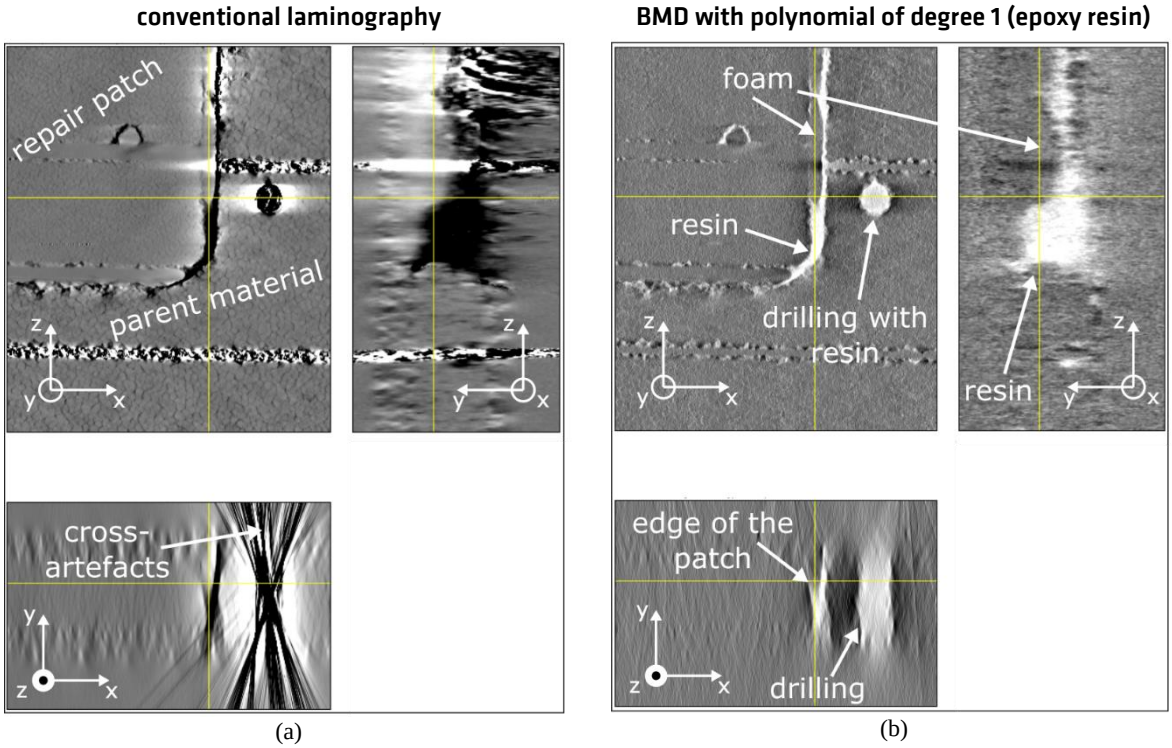

Fig. 13: Digital cross-sections through the reconstructed 3D volume from the laminographic scan. (a) Conventional laminography and (b) epoxy resin. Bright areas indicate a high amount of the present basis material.

The results also show an inherent drawback of the laminography as a 3D-reconstruction technique: No structures parallel to the scanning (x-)direction can be reconstructed due to direction selective high-pass filtering in advance of the 3D-reconstruction. This can particularly be observed in Figures 11c and 12c at the horizontal resin channels which seem not to be filled with resin but which actually are.

The use of different fitting functions (as in Eq. (6) or (7)) on the one hand yields a better approximation of the function with the sampling points but on the other hand results in a less stable equation system [17]. This in turn results in a high amount of salt-and-pepper noise after the BMD, especially in case of the conic function (Eq. (7)), and makes the results less accurate and reliable.

3. Conclusion

By using the spectral information of a photon counting detector and a suitable material reconstruction algorithm (*here:* basis material decomposition) the significance of a laminographic investigation on a wind turbine rotor blade shell could be increased. The material specific laminographic data sets revealed small voids, gaps between glass fiber bundles and lack of resin which were not detectable or not distinctly recognizable in the conventional laminographic data set. Heavy cross-artifacts in the conventional laminographic data set impeded a detailed investigation of the GFRP rotor blade shell segment since they overlaid structural information. These artefacts were suppressed by the material specific reconstruction using the BMD. The epoxy resin specific reconstruction shows unevenly distributed resin around the repair patch which results in an inhomogeneous connection between the repair patch and the parent structure. This method allows to detect damage and

evaluate repaired structures on wind turbine blades more reliably and therefore ensure the design lifespan of wind turbines to be reached. By using a mobile miniature X-ray tube and an appropriate manipulation system, this method might have the potential to be applied on-site offshore turbines.

Acknowledgments

The authors would like to acknowledge the financial support provided by National Natural Science Foundation of China (No. 51727813) and Tsinghua University Initiative Scientific Research Program.

We would also like to acknowledge Dustin Nielow for the preliminary work which became the basis of the rotor blade focus study within the LeBeWIND project at the BAM.

References

[1] A. Kupsch *et al.*, "X-ray laminographic inspection of sandwich shell segments for wind turbine rotor blades," in *Proceedings 12th European conference on Non-Destructive Testing*, 2018, pp. 1–8.

[2] F. Grasse, "Beitrag zur Untersuchung des Betriebsfestigkeitsverhaltens von Rotorblättern für Windenergieanlagen im verkleinerten Maßstab," Technische Universität Berlin, 2013.

[3] M. Gaal, F. Schadow, D. Nielow, and V. Trappe, "Air-coupled ultrasonic ferroelectret transducers with additional bias voltage for testing of composite structures," in *10th International Symposium on NDT in Aerospace*, 2018.

[4] V. Trappe and D. Nielow, "Fatigue Loading of Sandwich Shell Test Specimens with Simulated Production Imperfec-tions and In-situ NDT," in *Proceedings of 7th International Conference on Fatigue of Composites*, 2018.

[5] D. Schumacher, U. Ewert, and U. Zscherpel, "Influencing parameters on image quality using photon counting detectors for laminography," in *7th European-American Workshop on Reliability of NDE*, 2017, pp. 1–11.

[6] M. A. Caminero, S. Pavlopoulou, M. Lopez-Pedrosa, B. G. Nicolaisson, C. Pinna, and C. Soutis, "Analysis of adhesively bonded repairs in composites: Damage detection and prognosis," *Compos. Struct.*, vol. 95, pp. 500–517, Jan. 2013.

[7] D. J. Lekou and P. Vionis, "Report on Repair Techniques for composite parts of Wind Turbine blades," 2002.

[8] C. Ullberg, M. Urech, N. Weber, A. Engman, A. Redz, and F. Henckel, "Measurements of a Dual-Energy Fast Photon Counting CdTe Detector with Integrated Charge Sharing Correction," in *Medical Imaging 2013: Physics of Medical Imaging*, 2013, vol. Vol. 8668.

[9] K. Taguchi and J. S. Iwanczyk, "Vision 20/20: Single photon counting x-ray detectors in medical imaging," *Med. Phys.*, vol. 40, no. 10, 2013.

[10] D. Schumacher, U. Zscherpel, and U. Ewert, "Recent Developments of Photon Counting and Energy Discriminating Detectors for Radiographic Imaging," in *2017 Far East NDT New Technology & Application Forum (FENDT)*, 2018, pp. 281–285.

[11] B. G. Z. des Plantes, "Eine neue Methode zur Differenzierung in der Röntgenographie (Planigraphie)," *Acta radiol.*, vol. 13, no. 2, pp. 182–192, Mar. 1932.

[12] Andreas Deresch, K.-U. Thiessenhusen, U. Ewert, and C. Bellon, "Schneller Shift-Rekonstruktions-Algorithmus für die koplanare Translationslaminographie," in *DGZfP Jahrestagung*, 2014.

[13] K. Thiessenhusen, U. Ewert, B. Redmer, and K. Bavendiek, "Geometric Corrections in Coplanar Translational Laminography," in *International Symposium on Digital Industrial Radiology and Computed Tomography*, 2011, pp. 1–8.

[14] R. E. Alvarez and A. Macovski, "Energy-selective Reconstructions in X-ray Computerized Tomography," *Phys. Med. Biol.*, vol. 21, pp. 733–744, 1976.

[15] L. A. Lehmann, R. E. Alvarez, and W. R. Brody, "Generalized image combinations in dual KVP digital radiography," *Med. Phys.*, vol. 8 (5), pp. 659–667, 1981.

[16] H. N. Cardinal and A. Fenster, "An accurate method for direct dual-energy calibration and decomposition," *Med. Phys.*, vol. 17 (3), pp. 327–341, 1990.

[17] D. Ou, D. Schumacher, U. Zscherpel, and Y. Xiao, "Dual-energy materials characterization methods for laminography image enhancement based on photon counting detector," *J. Instrum.*, vol. 14, no. 02, p. P02018, Feb. 2019.